Nanoscale

ROYAL SOCIETY OF CHEMISTRY

PAPER

View Article Online
View Journal | View Issue

Cite this: *Nanoscale*, 2025, **17**, 16873

ZnO quantum dots as an electron-transport layer for highly efficient and stable organic solar cells†

Abdus Saboor,[a,b] Oleksandr Stroyuk,*[b] Oleksandra Raievska,[b] Chao Liu,*[b] Jens Hauch[a,b] and Christoph J. Brabec[a,b]

Received 27th April 2025,
Accepted 29th June 2025

DOI: 10.1039/d5nr01722j

rsc.li/nanoscale

An advanced protocol for the mild synthesis of stable and concentrated ZnO quantum dots (QDs) yields colloidal inks suitable for applications in electron-transport layers (ETLs) of organic solar cells, delivering superior power conversion efficiency (PCE) and photodegradation stability as compared to bulk-like commercially available ZnO inks. The champion ZnO QDs-based devices with a quaternary PM6 : L8BO : BTP-eC9 : $PC_{70}BM$ absorber exhibit a PCE of 18.86%, surpassing similar cells with bulk-like ZnO ETL (18.15%). The ZnO QDs exhibited size-dependent electron-transport efficiency, with the highest performance achieved for QDs of 4.4–4.5 nm, decreasing for larger QDs down to the level of the bulk-like ZnO reference. A correlation between the photoluminescence and electron-transport efficiencies of ZnO quantum dots (QDs) was observed and interpreted in terms of an interplay between the defect state density and exciton confinement in size-selected ZnO QDs.

1 Introduction

Photovoltaic (PV) conversion of solar energy is considered one of the pillars in the modern concept of a renewable energies-based economy, relying on many competing PV materials, including silicon, complex metal chalcogenides, organic bulk heterojunctions, and lead halide perovskites.[1] In this family, organic PV (OPV) stands unique, still retaining the status of an emerging PV technology and showing fast developments in efficiency and stability,[1,2] despite a solid 30–40-year-long research history.[1,3,4]

The current level of sophistication in the design of multi-component organic PV absorbers allowed the threshold of 20% power conversion efficiency (PCE) to be surpassed in 2024,[5] showing a large potential of organic PV still to be unveiled despite decades of continuous development.[2–4] These efficiencies and the complexity of the bulk heterojunction absorbers require the entire cell to be perfectly orchestrated with commensurate performances for other cell components, in particular, electron- and hole-transporting layers.

At that, the design of efficient and stable electron transport layers (ETLs) poses specific challenges. Typical ETL materials are inorganic oxides[6–8] that require relatively large thermal inputs for the crystallization and film densification. The oxide ETLs can form imperfect interfaces with organic absorbers, or induce degradative redox processes in the absorbers under UV illumination.[6–9]

Among the metal oxide ETLs, zinc oxide (ZnO) is one of the most broadly studied and applied materials, both for solar cells and light-emitting diodes (LEDs).[6,9] It combines excellent electron transport properties with a broad tunability of electronic structure, size, and shape of crystals, as well as a plethora of synthetic approaches available for the formation of thin ZnO films.[6–9] The OPV cells with ZnO ETLs exhibited an almost linear increase in PCE over the last 10–15 years, with no obvious signs of saturation,[8,9] indicating that ZnO has significant potential in further supporting the ever-growing efficiency of OPV absorbers. As of 2023, the efficiencies of OPV cells with ZnO ETLs surpassed 18% for single-junction devices and almost reached 20% for the organic–organic tandems.[9]

Despite the versatility of the approaches for ZnO ETL deposition, most reports focus on bulk or bulk-like ZnO ETLs composed of nanocrystals (NCs) larger than 10 nm, even when produced from colloidal inks,[9] most likely due to challenges in the reproducibility of the ETL properties for smaller sizes. The controlled variation of the ZnO NC size, especially in the

[a]*Friedrich-Alexander-Universität Erlangen-Nürnberg, Materials for Electronics and Energy Technology (i-MEET), Martensstrasse 7, 91058 Erlangen, Germany*
[b]*Forschungszentrum Jülich GmbH, Helmholtz-Institut Erlangen Nürnberg für Erneuerbare Energien (HI ERN), 91058 Erlangen, Germany.*
E-mail: o.stroyuk@fz-juelich.de

†Electronic supplementary information (ESI) available: Detailed description of ZnO QD synthesis, production and testing of PV devices, and characterizations; tabulated parameters of size-selected QD series and photodegradation tests; QD size calibration curve, XRD, DLS, and XPS results for ZnO QDs; details on optimization of the spectral and PV parameters of size-selected ZnO QDs; data on PV tests and photodegradation tests of PV cells with binary and ternary absorbers; exemplary energy diagram for a PV cell with ZnO QDs; detailed data on PV tests of solar cells with size-selected ZnO QDs as ETLs. See DOI: https://doi.org/10.1039/d5nr01722j

regime of spatial exciton confinement, typical for ZnO quantum dots (QDs) smaller than 6–7 nm,[8,9] poses an additional challenge. The latter is multiplied by the necessity of producing stable and concentrated inks with a minimal amount of external stabilizers that may compromise the conductivity of final ETLs.

Most probably, for these reasons, the reports on the application of size-selected ZnO QDs as ETLs, as well as on possible QD size effects on their performance in OPV cells, are quite rare.[8,9] Still, considering the strong influence of the spatial confinement in ZnO QDs on their photophysical and electrophysical properties, further exploration of the size effects on the charge transport and operational stability of OPV cells with nanocrystalline ZnO ETLs remains a topic of high relevance.

In the present report, we aim to address these challenges by introducing a mild, reproducible, and upscalable approach to colloidal ZnO QD inks. The method is based on stepwise solvent engineering on different stages, including the preparation of precursors, the formation of size-selected ZnO QDs, their precipitation for purification, and redispersion. The ZnO QD inks are stable and concentrated enough to be potentially applicable for the spin-coating or printing of ETLs in OPV devices, showing a prominent reproducibility of cell performance upon the storage of the QD inks. The OPV cells with ZnO QD ETLs revealed a superior performance combined with advanced photodegradation stability, suggesting good perspectives of these materials as an alternative to more conventional bulk-like ZnO ETLs.

2 Results and discussion

2.1 Synthesis and spectral properties of ZnO QD inks

The synthesis of colloidal ZnO QDs was performed at room temperature (RT) by reacting two precursors, the first produced by dissolving zinc acetate dihydrate in dry dimethyl sulfoxide (DMSO) and the second containing NaOH and traces of water in dry ethanol (EtOH). The precursor mixing initially yields a precipitate, presumedly $Zn(OH)_2$. This precipitate can spontaneously dissolve upon stirring, most probably due to the dehydration of $Zn(OH)_2$ by dry ethanol and the formation of ZnO QDs as a stable transparent colloidal solution. The presence of water traces is essential for the ZnO QDs to form, but a larger water content compromises the QD stability, and, therefore, the water content was varied as one of the optimization parameters.

The as-prepared ZnO ink was subjected to aging at 60 °C, followed by precipitation of the ZnO QDs with an antisolvent. The antisolvent was a mixture of hexane and toluene, with their ratio and volume optimized to minimize the presence of salt residuals in the final ink and maximize the ink stability upon storage. The precipitated ZnO QDs were then redispersed in dry EtOH containing traces of DMSO, which strongly contributed to the ink stability, most likely *via* binding to the undercoordinated Zn^{2+} ions on the QD surface. The final ZnO QD ink was stored in a refrigerator at approximately −20 °C, exhibiting perfect stability for many weeks. The details of the optimized procedures for the synthesis and purification of ZnO QD inks are presented in the ESI .† With all parameters kept constant, the optimized synthesis yields ZnO QD batches with highly reproducible properties – molar ZnO concentration and QD size (controlled by absorption spectroscopy), as well as ETL activity (controlled by a test in a standard 6-pixel solar cell with a binary absorber after the synthesis of each new batch of colloidal ZnO QDs).

Assuming that the QD precipitation by the antisolvent was complete (only residual photoluminescence (PL) of the QDs was observed in the supernatant as compared with the original ink), the molar concentration of the final ZnO QD ink was 0.3 M with respect to Zn^{2+} content or 0.25 M with respect to the nominal NaOH content. The commercial ZnO ink, supplied by Avantama and used as a reference in the present report, has a declared weight concentration of 2.5%, corresponding to a molar concentration of *ca.* 0.25 M.

Considering the large number of variables in the synthesis and purification of ZnO QD inks, a multi-parameter optimization of the synthesis was performed with two optimization criteria pursued – maximal PV activity and, simultaneously, maximal stability upon storage (evaluated as a period till QD aggregation and precipitation).

Three major parameters were found to affect the average size of ZnO QDs and strongly influence their PV activity: (i) the temperature of thermal aging (annealing) after the precursor mixing, T_{ag}, (ii) the duration of thermal aging at a certain temperature, and (iii) the ratio of molar concentrations of NaOH and $ZnAc_2$, [NaOH]/[$ZnAc_2$]. The size variation of ZnO QDs is summarized in the ESI (Table S1),† while the size effects on the activity of ZnO QDs as ETL are discussed in detail in section 2.3.

The size variation of ZnO QDs is exemplified in Fig. 1 for the series with varied aging temperatures. The colloidal ZnO QD inks show continuous absorption bands with distinct edges shifted to shorter wavelengths (Fig. 1a, lower panel, curves 1–5) as compared to the band edge of commercial ZnO ink (curve 6). This "blue" shift originates from the spatial exciton confinement in colloidal ZnO QDs and the size dependence of the bandgap.

Following the well-established approach,[10,11] the average bandgap in the QD ensembles can be evaluated from the position of a minimum of the first derivative of the absorption spectrum (Fig. 1, upper panel). The bandgap of ZnO QDs was found to shift from 3.66 eV for T_{ag} = 22 °C (RT) to 3.45 eV for T_{ag} = 60 °C. Further elevation of T_{ag} resulted in a loss of aggregation stability of ZnO QDs. The reference ZnO ink showed the bandgap at 3.34 eV (Fig. 1a, curve 6), corresponding to the bandgap range reported for bulk hexagonal zinc oxide.[10–13]

The average bandgap of ZnO ink can be used to evaluate the average size of ZnO QDs using well-established "E_g – size" relationships,[11,12] in particular, the sizing curve presented in ESI (Fig. S1).† Using this approach, the average size of ZnO QDs was found to evolve from 3.5 nm for RT to 4.6 nm for T_{ag} = 60 °C (ESI, Table S1†). Evaluations of the average QD size

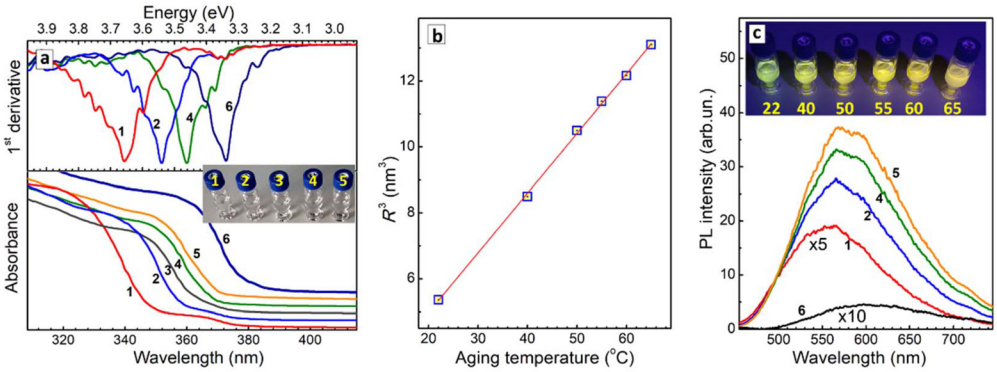

Fig. 1 (a and c) Absorption (a) and photoluminescence (c) spectra of ZnO QD inks (curves 1–5) produced at different aging temperatures, 22 °C (curves 1), 40 °C (2), 50 °C (3, only absorption spectrum shown), 55 °C (4), and 60 °C (5), and reference commercial ZnO ink (curves 6); in (a): lower panel shows original absorption spectra, upper panel – first derivatives of absorption spectra, the spectra are offset by *Y* axis; inserts in (a and c): photographs of ZnO QD inks under ambient illumination (a) and under UV illumination (c), numbers in (c) indicate aging temperature; (b) dependence of R^3 (R – average QD radius) of colloidal ZnO QDs on the aging temperature.

made from the absorption spectra were validated for the samples produced at 22 °C and 65 °C by the dynamic light scattering (DLS) measurements in colloidal solutions and X-ray diffraction (XRD) measurements on ZnO QD films deposited on glass substrates from the corresponding solutions. The average volumetric hydrodynamic size L of QDs was found to grow from 3.7 nm to 4.8 nm with an increase in annealing temperature from 22 °C to 65 °C (ESI, Fig. S2a†). The XRD patterns of the QD films produced from the same samples have a relatively low signal-to-noise ratio (ESI, Fig. S2b†) due to the low film thickness, but still allow the QD size D to be estimated from the broadening of XRD peaks as 3.4 ± 0.3 nm for 22 °C and 4.5 ± 0.3 nm for 65 °C. Both DLS and XRD showed a reasonably good correspondence with the estimations of the average QD size from absorption spectra.

The average volume of QDs expressed as R^3 (R – average radius of QDs assumed to be spherical) scales linearly with aging temperature (Fig. 1b), indicating that the Ostwald ripening governs the QD growth during the thermal treatment.[11,13,14] In this mechanism, larger QDs in the ensemble grow at the expense of the mass transfer from smaller QDs, resulting in a larger average size, narrower size distribution, and more ordered and less defective surface layer of QDs after the annealing. The latter effect is corroborated by the gradual growth of PL intensity with increasing T_{ag} (Fig. 1c). In general, the ZnO QDs reveal 1–2 orders of magnitude higher PL efficiency as compared to reference bulk-like ZnO ink, indicative of much lower non-radiative losses of charge carriers in ZnO QDs.

Evolution of the surface chemistry of ZnO QDs during annealing was additionally probed by X-ray photoelectron spectroscopy (XPS) for the starting sample produced with no annealing and for the ZnO QD sample aged at 65 °C. The most prominent differences in the XPS spectra of both samples are observed in the range of Zn2p electron binding energies (ESI, Fig. S3†). The Zn2p doublet of the non-aged sample can be approximated by two pairs of Gauss curves centered at 1021.5/1044.5 eV and 1022.0/1045.0 eV, assigned to ZnO and $Zn(OH)_2$, respectively.[15] Both pairs of doublet signals are separated by 23 eV, typical for $2p^{3/2}$ and $2p^{1/2}$ signals of zinc.[15] The ratio of integral intensities of ZnO-related and $Zn(OH)_2$-related peaks was found to be 2.0 : 1 ($2p^{3/2}$) and 2.5 : 1 ($2p^{1/2}$), indicating that the dehydration of the $Zn(OH)_2$ precursor in the non-aged sample is incomplete with 25–30% of Zn^{2+} still bound with OH^-, most probably forming a surface layer of ZnO QDs. On the contrary, the sample annealed at 65 °C shows a single pair of symmetric peaks at 1021.5 eV and 1044.5 eV, typical for ZnO, indicating a much deeper thermal transformation of Zn$(OH)_2$ into zinc oxide. These observations agree with the PL enhancement during the aging and indicate gradual elimination of the surface defects, in particular, under-dehydrated $Zn(OH)_2$ species.

A similar evolution of the average bandgap and size of ZnO QDs is observed for varied aging durations with a fixed aging temperature (ESI, Fig. S4a†). In an exemplary case of T_{ag} = 60 °C and the aging time varied from 0 to 15 min, the average size of ZnO QDs grows from 3.7 to 5.0 nm (ESI, Fig. S4b; Table S1†), followed by a concomitant growth of PL intensity (Fig. S4c†).

An increase in the [NaOH]/[$ZnAc_2$] ratio from 0.6 to 1.4 also results in the bandgap narrowing (ESI, Fig. S5a†) and a growth of the average QD size from 3.9 nm to 5.2 nm (Fig. S3b†). The ZnO QD inks produced with [NaOH]/[$ZnAc_2$] > 1.4 are unstable, indicating that QDs are stabilized by surface complexes of Zn^{2+}. The size decrease at lower NaOH contents can be understood in terms of a larger surface charge, resulting in lower QD growth rates and higher electrostatic repulsion between QDs.

The ZnO QDs revealed size-dependent PV activity, as discussed in detail in section 2.3. The best balance between the PV activity and stability during storage was found for the ZnO QD sample with an average size of *ca.* 4.5 nm produced with the following set of parameters: aging temperature of 60 °C, aging duration of 10 min, and [NaOH]/[$ZnAc_2$] = 1.4. Section 2.2 focuses on the details of the PV performance of the solar cells with this particular (optimized) ZnO QD sample.

Other parameters of the synthesis/purification were found to have no significant effect on the average size and only marginal effects on the performance of ZnO QDs as ETL. These parameters include (i) EtOH/DMSO ratio during the synthesis and re-dispersion (ESI, Fig. S6†), (ii) antisolvent volume (ESI, Fig. S7†), and (iii) hexane/toluene ratio in the antisolvent (ESI, Fig. S8†). Similar to the size-varied series, for these parameters, a balance between the PV performance and the long-term ink stability was found, resulting in the optimized ink synthesis protocol (see ESI for details†) used to produce the ETL materials optimal in terms of efficiency and stability as discussed in Section 2.2.

2.2 Performance of optimized ZnO QDs as ETL for organic solar cells

The optimized ZnO QD ink was tested as an ETL component in OPV solar cells with three different state-of-the-art donor/acceptor absorbers of increasing complexity – (i) binary PM6 : L8BO (see structures and IUPAC names in ESI, Fig. S9†), (ii) ternary PM6 : L8BO : $PC_{70}BM$ (ESI, Fig. S10†), and (iii) quaternary PM6 : L8BO : $P_{70}BM$: BTP-eC9 (ESI, Fig. S11†). The ZnO ETL layers were deposited by the spin-coating of the inks on pre-cleaned patterned glass/ITO substrates and subjected to annealing at 200 °C both for ZnO QDs and the reference ETL. More details can be found in the ESI.†

A scanning electron microscopic (SEM) survey of ZnO QD films showed them to be macroscopically uniform and formed by randomly aggregated ZnO grains with an average size of *ca.* 5 nm (Fig. 2a, i–iii), in accordance with the spectral estimations. Annealing increases the uniformity of the QD film and reduces the density of the pinholes, favoring the contact with absorbers. In contrast, the films of reference ZnO showed a broad distribution of larger grain sizes from below 10 nm to 30 nm (Fig. 2b, i–iii), with the film morphology not affected considerably by the annealing.

The thickness of the reference ZnO ETL evaluated by cross-sectional SEM is *ca.* 30 nm (Fig. 2b, iv). As the single spin-coating deposition of the ZnO QDs typically produces a thinner layer of *ca.* 15 nm, the deposition of ZnO QD ink was repeated twice before the annealing to form a *ca.* 30 nm-thick ZnO QD layer (Fig. 2a, iv) and match the thickness of the reference ZnO ETL.

The ZnO QD ETLs were tested in inverted OPV devices with a device configuration of ITO/ETL/active layer/MoO_x/Ag (Fig. 3a). The active layers were deposited by spin-coating on the freshly annealed ITO/ZnO substrate, followed by the thermal evaporation of a layer of molybdenum oxide (MoO_x) as a hole transport layer (HTL) for binary and ternary absorbers, or a commercially available BM-HTL-1 layer (Brilliant Matters) for the quaternary absorber. The preparation of the cells was finalized by the thermal evaporation of silver back electrodes. All deposition parameters were kept identical for ZnO QD- and reference ZnO-based cells. The final devices contained *ca.* 160 nm ITO support, *ca.* 30 nm ZnO ETL, *ca.* 100 nm absorber layer, and *ca.* 140 nm layer of HTL/Ag (see insert in Fig. 3a).

The work functions of ZnO reference ETL, as well as ETLs produced from ZnO QDs with the average QD size of 3.5 nm (RT) and 4.6 nm (aging at 60 °C), were evaluated by Kelvin probe measurements as −4.2 ± 0.1 eV, −4.3 ± 0.1 eV, and −4.4 ± 0.1 eV, respectively. Considering the error margin, the work function showed a rather insignificant dependence on the ZnO crystal size, in accordance with the experimentally observed small variations of V_{oc} (within 5–10 mV) in all series with size-selected ZnO QDs (see discussion below and ESI, Fig. S20, S21, and S22†). Fig. S12 in ESI† shows an exemplary energy level diagram for the cells with different ITO/ZnO ETLs, a binary PM6 : L8BO absorber, MoO_x HTL, and Ag back electrode.

For all tested absorber compositions, the cells with ZnO QDs showed a higher average PCE as compared to the similar cells with the reference bulk-like ZnO ETL (Table 1).

In the case of the binary absorber, this difference is marginal, 15.10% *versus* 15.07%; however, it increases for the ternary absorber, 16.18% *versus* 15.65%, and especially for the quaternary absorber, 18.15% *versus* 17.36%.

The distribution of PCEs for ZnO QD-based cells (Fig. 3b, red bars, plotted for 36 single devices) is narrower and shifted

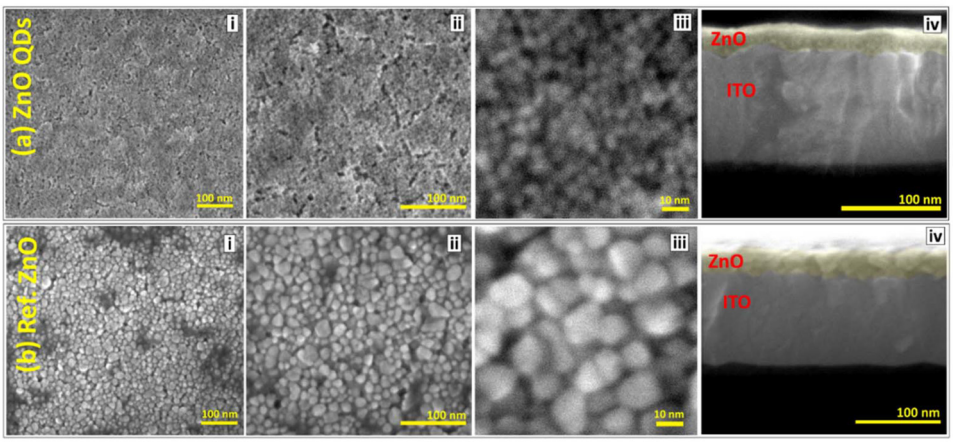

Fig. 2 Frontal (i–iii) and cross-sectional (iv) images of ZnO film on ITO produced from ZnO QD ink (a) and reference bulk-like ZnO ink (b).

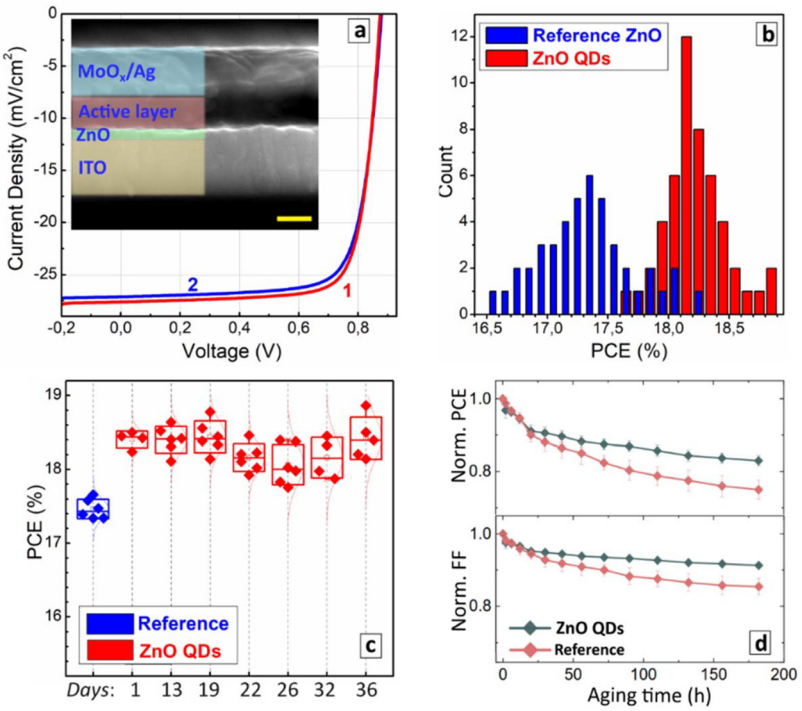

Fig. 3 (a) Current–voltage curves for "champion" solar cells with quaternary active layer (see Table 1) and ETL = ZnO QDs (curve 1) and ETL = reference ZnO (2); insert shows a cross-sectional SEM image of the champion cell with ZnO QDs as ETL; scale bar is 100 nm; (b) statistical distribution of PCE values collected for solar cells with the quaternary active layer and ETL = ZnO QDs (red bars) and ETL = reference ZnO (blue bars); (c) PCE distributions collected for the cells with the quaternary active layer and ETL produced from reference ZnO as well as from ZnO QD inks stored at −20 °C for different periods; (d) evolution of average normalized PCE and FF of the cells with the binary active layer and ZnO ETLs under 5-sun "white" LEDs illumination.

Table 1 PV performance of solar cells with different absorbers and ZnO ETLs

Active layer	ETL	$\lvert J_{sc}\rvert$ (mA cm^{-2})	V_{oc} (mV)	FF (%)	PCE (%)
Binary PM6 : L8BO	ZnO QDs	23.43	845	76.30	15.10
	Reference	23.39	856	75.10	15.07
Ternary PM6 : L8BO : $PC_{70}BM$	ZnO QDs	24.32	881	75.80	16.18
	Reference	23.44	882	75.90	15.65
Quaternary PM6 : L8BO : $PC_{70}BM$: BTP-eC9	ZnO QDs	27.30 (27.60)*	875 (875)*	76.30 (78.20)*	18.15 (18.86)*
	Reference	26.68 (27.11)*	870 (875)*	75.10 (76.00)*	17.36 (18.15)*

Values with an asterisk are presented for the "champion" solar cell. The accuracies of J_{sc}, V_{oc}, FF, and PCE measurements are 0.01 mA cm^{-2}, 1 mV, 0.01%, and 0.01%, respectively.

to higher PCEs as compared to the PCE distribution of the reference cells (Fig. 3b, blue bars, plotted for 44 single devices), indicating a statistically significant difference in performance. Particular PV parameters show significant differences in the distributions of the short-circuit current J_{sc} (ESI, Fig. S13a†) and the fill factor FF (ESI, Fig. S13c†). The distributions of the open-circuit voltage V_{oc} of the tested and reference samples overlap (ESI, Fig. S13b†); however, the cells with ZnO QD ETL show a much narrower distribution, attesting to a higher control over the device performance.

The "champion" device with the quaternary absorber and ZnO QD ETL showed a PCE of 18.86% (see Table 1 and exemplary *J–V* curves in Fig. 3a), while the maximal PCE reached with the reference ZnO ETL was 18.15%. The examples of the comparative performance of ZnO QDs and the reference for binary and ternary absorbers are presented in the ESI (Fig. S9 and S10).†

The colloidal ZnO QD inks yield reproducible performance as ETL when stored for many days in closed vials in the dark at *ca.* −20 °C. Periodical testing of the same batch of colloidal ZnO QD inks during many days of storage showed very similar performance of the OPV devices produced with the freshly prepared ink and with the same ink stored for 13 to 36 days (Fig. 3c and ESI, Fig. S11†). The reproducibility of PV parameters indicates a high level of QD stabilization against precipitation and QD size evolution achieved in the ZnO QD ink without any additional ligands.

In addition to perfect stability and higher performance, the cells with ZnO QD ETL are typically more stable to photodegradation as compared to similar devices with the reference bulk-like ZnO ETL. The cells with the binary absorber and ZnO QDs, taken as an example, retain more than 80% of the original PCE after the exposure for 180 h, showing a significantly higher stability than the reference (Fig. 3d; the non-normalized data are presented in ESI, Fig. S14†). The cells with ternary and quaternary absorbers showed similar dynamics during the photodegradation, both for the QD-based and reference devices (see exemplary data for the ternary absorber in ESI, Fig. S15†).

Evolution of normalized FF (Fig. 3d), J_{sc}, and V_{oc} (ESI, Fig. S16†) indicates that the photodegradation mostly affects FF, the cells with the ZnO QD ETL retaining *ca.* 90% of the original value after the stability test. These observations indicate that ZnO QDs form a much more stable interface with the organic absorber, probably due to the lower density of surface traps in QDs as discussed above, as well as a lower inherent photoactivity.

The higher quality of the ZnO/absorber interface in the case of ZnO QDs is additionally supported by the evaluations of serial (R_s) and shunt (R_{sh}) resistances (ESI, Table S2†) from "light" and "dark" *J*–*V* curves registered before and after the photodegradation test (ESI, Fig. S17†). The binary-absorber cells showed almost twice lower R_s values in both cases, while R_{sh} was found to be an order of magnitude higher for ZnO QDs as compared to the reference ETL. The photodegradation resulted in a 6-times drop in R_{sh} for the reference cells, while decreasing R_{sh} slightly more than by half for ZnO QD-based devices (ESI, Table S2†).

The superior performance of the ZnO QD ETL potentially allows the ETL layer to be much thinner as compared to the reference devices. It was found that the quaternary-absorber cells with a single deposition of ZnO QDs (layer thickness of *ca.* 15 nm) perform as well as the devices with a double ZnO QD layer (ESI, Fig. S18†), the latter produced to match the thickness of the reference ZnO ETL (Fig. 2a and b, iv). The deposition of the third QD layer results in a decrease of PV performance, most probably due to an excessively large hopping distance for electrons in such layers.

Similar effects were also observed with variations of the QD concentration, achieved by varying the volume of EtOH for the redispersion of ZnO QDs after the purification. At that, more concentrated ZnO QD inks resulted in lower efficiency (ESI, Fig. S19†), most probably due to the excessive thickness of the final ETL layer.

2.3 Size effects on the performance of ZnO QDs as ETL

As discussed in section 2.1, variations of three key parameters of the QD synthesis were found to affect the average QD size, namely, the temperature and duration of aging and the [NaOH]/[$ZnAc_2$] ratio. The three series of size-selected QD inks were tested as ETL components in the solar cells with the quaternary absorber and, taken together, revealed a distinct effect of the average size of ZnO QDs on the PV performance. A summary of the synthesis conditions, average sizes of ZnO QDs, and PV parameters of the corresponding devices can be found in the ESI, Table S1.†

The effect of the ZnO QD size on the cell efficiency is illustrated by a series of QDs prepared at different aging temperatures (Fig. 4a and ESI, Fig. S20†). The QDs produced at T_{ag} = 22 °C, with an average QD size of 3.5 nm (ESI, Table S1†), showed an average PCE of 16.2% with "champion" devices approaching the PCE of a solar cell with the reference ZnO.

The average size of ZnO QDs and their activity as ETL material grow with the increase of T_{ag} up to 55 °C. Above this threshold, at T_{ag} = 60–65 °C, the colloidal QD ink shows an inferior stability, and the PCE of final devices decreases (Fig. 4a). Both J_{sc} and FF reveal this size-dependent behavior as well, contributing to the variation in PCE, while V_{oc} remains almost unaffected by the QD size variations (ESI, Fig. S20†).

Similar trends are observed at the variations of the annealing duration for a fixed T_{ag} (ESI, S21†) and the [NaOH]/[$ZnAc_2$] ratio (ESI, Fig. S22†). The QD-based cells demonstrate an increase in efficiency till an optimal size of QDs is reached, and lower PCEs at larger QD sizes.

Fig. 4b summarizes the size dependencies of the average PCE for all three size-selected series, with more details on specific PV parameters (J_{sc}, V_{oc}, and FF) shown in the ESI (Fig. S23†).

The series on annealing temperature and duration show a steady growth of PCE as the average size is increased from 3.5 to 4.4–4.5 nm followed by a decrease in the efficiency for larger sizes until the level of PV activity of the reference ZnO ETL is achieved (Fig. 4b). The series with varied [NaOH]/[$ZnAc_2$] ratios follows the same trend but shows lower activities for the sizes larger than 4.5 nm, as compared to other series. As larger ZnO QDs in this series were produced at higher concentrations of NaOH, the drop in activity can be related to the excessive charging of the QD surface with OH^- anions, resulting in the increased electrostatic repulsion barrier for electron transport.[16,17] Taken together, all three size-selected series show a clear maximum in the efficiency of ZnO QDs as ETL for sizes around 4.5 nm, with this gain in efficiency gradually decreasing for larger QDs.

To get insights into the effect of the ZnO QD size on the electrical parameters of the cells, "dark" *J*–V curves were analyzed for the series of quaternary-absorber-based devices with size-selected ZnO QDs produced at different annealing temperatures (Fig. 5a). The cells were identical in terms of the composition, number, order, and thickness of all layers, differing only in the average size of ZnO QDs in the ETL. For this reason, variations in the conductivity of these devices can be directly related to size effects in the ZnO ETL. With known cell area and cell thickness evaluated by the cross-sectional SEM (Fig. 3a, insert), the resistivity and conductivity of the cells can be determined from the current density taken at an arbitrary voltage within the linearly rising section of the *J*–*V* curves, for example, at V = 1.5 V.

The conductivity of the cells was found to increase by a factor of two, from 3.0×10^3 S cm^{-1} for $\langle d \rangle$ = 3.5 nm (no aging)

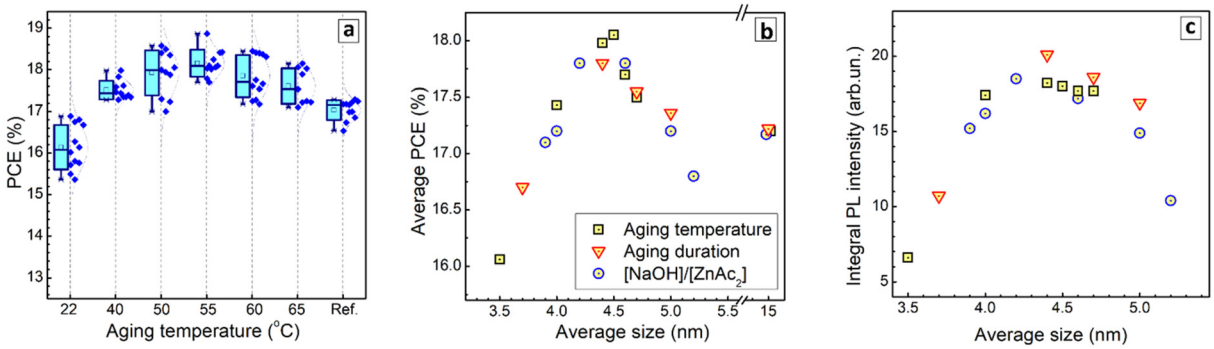

Fig. 4 (a) PCE distributions for solar cells with the quaternary absorber and ZnO QDs produced at different aging temperatures. (b and c) Average PCE (b) and integral PL intensity (c) as functions of the average size of ZnO QDs for three size-selected series of samples.

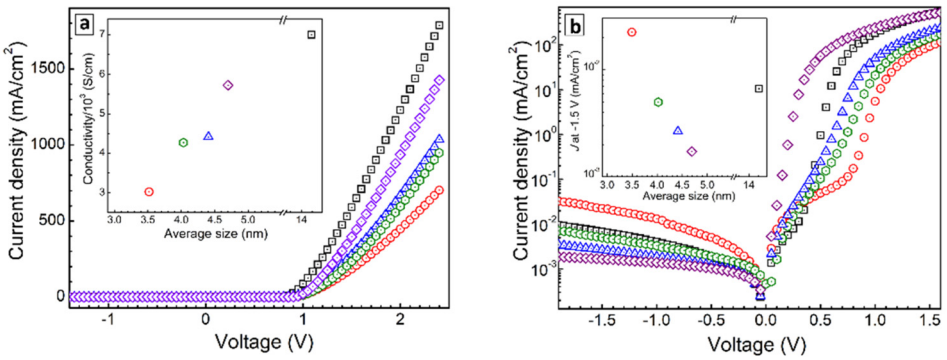

Fig. 5 "Dark" *J*–*V* curves of solar cells with the quaternary absorber and ZnO ETL produced from size-selected QDs and commercial reference presented as normal (a) and semilogarithmic (b) plots. Inserts show the conductivity of the cells measured at +1.5 V (a) and current density at −1.5 V (b) as functions of the average ZnO NC size.

to 5.8×10^3 S cm^{-1} for $\langle d \rangle$ = 4.7 nm (T_{ag} = 65 °C), gradually approaching the conductivity of the reference cells, 7.0×10^3 S cm^{-1} (Fig. 5a, insert). Given the fact that the conductivity of the best-performing cells with the average ZnO QD size of 4.4–4.5 nm is *ca.* 50% lower than that of the reference cells, it cannot be taken as a decisive factor, which alone determines the size-dependent performance of the nanocrystalline ZnO ETLs.

The "dark" *J*–*V* curves presented in semilogarithmic coordinates (Fig. 5b) show considerable differences in the "dark" currents at negative bias. In particular, the current density measured at an arbitrary voltage of −1.5 V was found to decrease by an order of magnitude with an increase of the aging temperature from 22 °C ($\langle d \rangle$ = 3.5 nm) to 65 °C ($\langle d \rangle$ = 4.6 nm, Fig. 5b, insert).

While the cells with non-annealed ZnO QDs as ETL show inferior diode behavior as compared to the reference, the cells with 4.4–4.7 nm ZnO QDs as ETL demonstrate "dark" current densities by a factor of *ca.* 3 lower than that of the reference. This trend is in line with the PL variations and can be interpreted by the gradual elimination of trap states, for example, Zn–OH species, as shown above by XPS, as well as by deeper ordering of the QD lattice and surface layer during the annealing.

The electron-transport efficiency of ZnO QDs was found to correlate with the efficiency of PL emission, which also shows a volcano-shaped size dependence, with the most emissive samples having the average size of 4.3–4.4 nm (Fig. 4c). The broadband PL emission of ZnO QDs is typically associated with the radiative recombination of one or both charge carriers trapped by mid-gap states.[11,17,18] At that, the PL is characterized by relatively large average lifetimes, *ca.* 1 μs for the size range of 4–5 nm,[19] indicative of strongly depressed non-radiative recombinative processes in such QDs.

The volcano-shape of the size dependence of PL efficiency can originate from an interplay of two opposite trends – (i) PL enhancement with increasing QD size due to the thermal annealing of defects and lattice ordering and (ii) gradual lowering of the probability of the radiative recombination due to weaker exciton confinement in larger ZnO QDs.[11,17,18]

At that, maximum PL efficiency is observed for $\langle d \rangle$ = 4.4–4.5 nm, which are annealed at 50–55 °C (ESI, Table S1†), but still small enough to be comparable with the Bohr diameter of exciton in ZnO, resulting in weak quantum confinement of the charge carriers and higher probability of the radiative recombination due to the spatial localization of the charge carriers. The highest PL efficiency of the 4.4–4.5 nm ZnO QDs indicates the lowest probability of the non-radiative electron–

hole recombination and, therefore, minimal non-recombinative losses of charge carriers in such material, when applied as an electron-selective component of the solar cells. Due to the spatial confinement, the wave function of an electron injected into ZnO QDs extends both into the QD volume and on the surface, making the volume and surface transport mechanisms[16] simultaneously possible.

In these terms, negligent PL emission by the bulk-like reference ZnO can be interpreted by both the presence of the under-annealed radiative recombination centers and the lack of quantum confinement.

Recently, it was reported that the depth of radiative states in the bandgap has almost no effect on the conductivity of nanocrystalline ZnO films;[20] however, the relationships between the defect density (PL intensity) and the charge transport efficiency in solar cells were not discussed in detail. Earlier observations indicated a detrimental effect of non-emissive surface traps on the charge transport in nanocrystalline ZnO films.[16] Later, a positive correlation between the electron injection rate from ZnO QDs and the intensity of their PL was reported for QD-based LEDs with ZnO as ETL.[21]

In general, the influence of defect states on the electron transport in nanocrystalline ZnO solids can be directly related to and assessed by their PL behavior. In opposite, the effects of the spatial electron localization in ZnO QDs on their transport properties are far from being well understood and require dedicated experimental and theoretical investigations, going beyond the scope of the present report.

The correlation between the PL intensity and electron-transport activity of ZnO QDs can alternatively be explained by the participation of the mid-gap defect states in the charge transport. The possibility of electron hopping through the mid-gap states in nanocrystalline ZnO was indeed discussed for the nanocrystalline ZnO ETLs as a transport channel complementary to the conduction-band-mediated electron transport.[17] This additional transport channel can result in an advanced activity of ZnO QDs as an ETL component as compared to the non-emissive bulk-like reference ZnO with a low population of radiative charge traps.

In light of the above discussion, the decrease of the ETL activity observed in the present work for the QD sizes lower than 4.4–4.5 nm can be accounted for by several reasons. First, smaller QDs show a lower PL intensity, indicating a higher population of non-radiative traps. Second, the electron transport through the QD layer meets an injection barrier, growing inversely proportional to the size in the spatial exciton confinement regime, as reported for ZnO QDs[17] and other semiconductor QDs.[22] Finally, smaller QDs have a larger surface-to-volume ratio and, therefore, a larger negative potential created by the surface layer of OH^- anions.[17]

In general, considering multiple factors that can affect the electron transfers in ZnO QDs, other alternative explanations may not be excluded, both for the higher activity of 4.4–4.5 nm ZnO QDs as compared with the bulk zinc oxide and for the gradual loss of this superiority at smaller QD sizes.

3 Conclusions

An advanced protocol for the mild synthesis of size-variable ZnO QDs is proposed, based on the solvent engineering for specific steps of the preparation of precursors, QD formation, post-synthesis QD deposition, and redispersion. It reproducibly yields stable and concentrated colloidal inks ready for applications in printed electronic devices.

The ZnO QD inks were tested as ETLs in organic solar cells with several types of donor/acceptor absorbers (from binary to quaternary compositions) and compared with a bulk-like ZnO ETL reference. The synthesis parameters of ZnO QDs were then optimized to achieve the highest PV activity of the final cells, the highest stability of the QD ink, and the reproducibility of the synthetic protocol.

The solar cells based on the optimized ZnO QDs revealed higher PCEs for all types of absorbers, higher or equal stability during the standard photodegradation tests, as well as high reproducibility of cell performance upon long-term storage of the ZnO QD inks. The most efficient solar cells with the quaternary PM6 : L8BO : P_{70}BM : BTP-eC9 absorber show average PCEs of 18.15% and 17.36% and "champion" PCEs of 18.86% and 18.15% for the ZnO QD ETL and reference bulk-like ZnO ETL, respectively.

The ZnO QDs exhibited size-dependent electron-transport efficiency, with the highest performance achieved for QDs of 4.4–4.5 nm, decreasing for larger QDs down to the level of the bulk-like ZnO reference. The cells with the most efficient ZnO QD ETL showed "dark" conductivities comparable to those of the reference-based cells, but revealed an enhanced rectification behavior, indicative of a lower defect density.

A distinct correlation is observed between the PL emission and electron-transport activity of ZnO QDs, both reaching the highest values for 4.4–4.5 nm ZnO QDs. The size dependencies of the PL efficiency and activity of ZnO QDs as an ETL were interpreted as results of the lowest probability of the non-radiative processes, including the non-radiative electron–hole recombination, for this particular size range and annealing conditions. The optimum is assumed to originate from a favorable combination of the low defect density and high QD lattice perfection achieved by the annealing, with the weak exciton confinement regime promoting both radiative electron–hole recombination and electron transport by suppressing competitive non-radiative pathways.

Author contributions

A. Saboor: investigation (lead), methodology (equal), writing – review & editing (equal); O. Stroyuk: conceptualization (lead), writing – original draft preparation (lead); O. Raievska: investigation (equal), methodology (lead); writing – review & editing (equal); C. Liu: conceptualization (equal); investigation (equal), writing – review & editing (equal); J. Hauch: project administration (lead), writing – review & editing (equal); C.J. Brabec: conceptualization (equal), funding acquisition (lead), writing – review & editing (equal).

Conflicts of interest

There are no conflicts to declare.

Data availability

The data supporting this article have been included as part of the ESI.†

Acknowledgements

A. S. acknowledges the Deutscher Akademischer Austausch-Dienst (DAAD) scholarship for financial support for his Ph.D study at i-MEET and HIERN. C. L. gratefully acknowledges the financial support through the Helmholtz Association in the framework of the innovation platform "Solar TAP", under grant agreement No. 952911 ("BOOSTER") and 101007084 ("CITYSOLAR").

References

1 P. K. Nayak, S. Mahesh, H. J. Snaith and D. Cahen, *Nat. Rev. Mater.*, 2019, **4**, 269.
2 G. Zhang, F. R. Lin, F. Qi, T. Heumüller, A. Distler, H. J. Egelhaaf, N. Li, P. C. Y. Chow, C. J. Brabec, A. K. Y. Jen and H. L. Yip, *Chem. Rev.*, 2022, **122**, 14180.
3 B. Kippelen and J. L. Bredas, *Energy Environ. Sci.*, 2009, **2**, 251.
4 O. Inganäs, *Adv. Mater.*, 2018, **30**, 1800388.
5 H. Chen, Y. Huang, R. Zhang, H. Mou, J. Ding, J. Zhou, Z. Wang, H. Li, W. Chen, J. Zhu, Q. Cheng, H. Gu, X. Wu, T. Zhang, Y. Wang, H. Zhu, Z. Xie, F. Gao, Y. Li and Y. Li, *Nat. Mater.*, 2025, **24**, 444.
6 X. Liang, S. Bai, X. Wang, X. Dai, F. Gao, B. Sun, Z. Ning, Z. Ye and Y. Jin, *Chem. Soc. Rev.*, 2017, **46**, 1730.
7 B. Yang, J. Cang, Z. Lia and J. Chen, *Nanoscale Adv.*, 2024, **6**, 1331.
8 C. Liu, C. Xiao and W. Li, *J. Mater. Chem. C*, 2021, **9**, 14093.
9 Y. Han, J. Guo, Q. Luo and C. Q. Ma, *Adv. Energy Sustainability Res.*, 2023, **4**, 2200179.
10 N. S. Pesika, K. J. Stebe and P. C. Searson, *J. Phys. Chem. B*, 2003, **107**, 10412.
11 S. Monticone, R. Tufeu and A. V. Kanaev, *J. Phys. Chem. B*, 1998, **102**, 2854.
12 V. A. Fonoberov and A. A. Balandin, *Phys. Rev. B*, 2004, **70**, 195410.
13 E. M. Wong, J. E. Bonevich and P. C. Searson, *J. Phys. Chem. B*, 1998, **102**, 7770.
14 R. Viswanatha, P. K. Santra, C. Dasgupta and D. D. Sarma, *Phys. Rev. Lett.*, 2007, **98**, 255501.
15 A. V. Naumkin, A. Kraut-Vass, S. W. Gaarenstroom, C. J. Powell and A. Y. Lee, NIST X-ray Photoelectron Spectroscopy Database, Version 5.0, 2023, DOI: **10.18434/T4T88K**.
16 E. A. Meulenkamp, *J. Phys. Chem. B*, 1999, **103**, 7831.
17 M. Shokrani, D. Scheunemann, C. Göhler and M. Kemerink, *J. Phys. Chem. C*, 2025, **129**, 611.
18 O. L. Stroyuk, V. M. Dzhagan, V. V. Shvalagin and S. Ya. Kuchmiy, *J. Phys. Chem. C*, 2010, **114**, 220.
19 O. Raievska, Ya. Panasiuk, O. Stroyuk, S. Kuchmiy, V. Dzhagan, A. Milekhin, N. Yeryukov, L. Sveshnikova, E. Rodyakina, V. Plyusnin and D. Zahn, *RSC Adv.*, 2014, **4**, 63393.
20 K. Yang, J. Fu, L. Hu, Z. Xiong, M. Li, X. Wei, Z. Xiao, S. Lu and K. Sun, *ACS Appl. Mater. Interfaces*, 2018, **10**, 39962.
21 J. Pan, J. Chen, Q. Huang, Q. Khan, X. Liu, Z. Tao, Z. Zhang, W. Lei and A. Nathan, *ACS Photonics*, 2016, **3**, 215.
22 M. S. Kang, A. Sahu, D. J. Norris and C. D. Frisbie, *Nano Lett.*, 2010, **10**, 3727.